Direct Probe of Molecular Polarization in *De Novo* Protein–Electrode Interfaces

Kendra Kathan-Galipeau, Sanjini Nanayakkara,[†] Paul A. O'Brian, Maxim Nikiforov,[‡] Bohdana M. Discher, and Dawn A. Bonnell*

Departments of Materials Science and Biophysics, The University of Pennsylvania, Philadelphia, Pennsylvania 19104, United States.
[†]Present address: National Renewable Energy Lab, Golden, Colorado 80401. [‡]Present address: 8300 28th Ct. NE suite 200, Lacey, Washington 98516.

ABSTRACT A novel approach to energy harvesting and biosensing devices would exploit optoelectronic processes found in proteins that occur in nature. However, in order to design such systems, the proteins need to be attached to electrodes and the optoelectronic properties in nonliquid (ambient) environments must be understood at a fundamental level. Here we report the simultaneous detection of electron transport and the effect of optical absorption on dielectric polarizability in oriented peptide single molecular layers. This characterization requires a peptide design strategy to control protein/electrode interface interactions, to allow peptide patterning on a substrate, and to induce optical activity. In addition, a new method to probe electronic, dielectric, and optical properties at the single molecular layer level is demonstrated. The combination enables a quantitative comparison of the change in polarization volume between the ground state and excited state in a single molecular layer in a manner that allows spatial mapping relevant to ultimate device design.

KEYWORDS: scanning impedance · peptide · protein · bio-optoelectronic · porphyrin · device · interface · scanning probe microscopy

Recently, the appreciation of the high energy yield and quantum efficiencies of a number of natural photoactivated proteins, in the context of a decade of research on molecular electronics, has raised the possibility of new nanoelectronic device applications. Bio-based strategies for light-activated electron pumps, solar cells, chemical sensors, and optoelectronics have been suggested. An obvious challenge is to understand and control the properties of the proteins when attached to electrodes and configured in the ambient environments relevant to potential device architectures. Two recent studies examined the surface potential of membranes extracted from plant systems on metal surfaces,[1,2] and STM or conductive AFM has been employed to characterize the conduction of some proteins on surfaces.[1,3,4] The ability to engineer simpler proteins with optoelectronic function enables control over assembly, interface connection, optical absorption properties, and conduction pathways.[5−14] However, to date, these proteins have been characterized in liquid environments.[15−17] Characterization of electronic, optical, and, importantly, dielectric property variations in proteins on substrates in ambient environments has not been reported.

Such characterization is not only a prerequisite to device applications but would provide a platform on which to enable significant advances in our understanding of natural photoactive systems. In this study, we combine peptide design, monolayer patterning, and a new probe of bio-optoelectronic function to characterize the dielectric and optoelectronic properties of an ambient protein–electrode system. We show that excitation of a photoactive protein complex on an electrode surface results in a quantifiable change in molecular polarization. The polarization volume in the excited state is found to be larger than in the dark state and is associated with the changes in orbital occupation within the peptide complex.

RESULTS

The past decade has witnessed significant advances in the design and synthesis of proteins with tailored properties.[5−17] This capability can be exploited to engineer proteins with simple structures that contain the functional components of natural counterparts, in configurations that enable experimental access, and device design. Here we synthesize new protein models, called maquettes, which are designed to transfer electrons, assemble on an electrodic substrate, and to possess optoelectronic activity. The interior of the artificial protein scaffolding is used to control the position, orientation, and properties of cofactor(s), which in this case are chosen for specific optical properties (absorption wavelength

* Address correspondence to bonnell@lrsm.upenn.edu.

Received for review March 7, 2011 and accepted May 25, 2011.

Published online May 25, 2011
10.1021/nn200887n

and excited state lifetime). The exterior of the scaffolding can be used to control the peptide's supramolecular assembly. The maquette used here consists of amphiphilic helices that self-assemble in detergent solution to form 4-helix bundles (Figure 1).[12,13] It was designed to possess distinct hydrophobic and hydrophilic domains along the length of the exterior of the bundle. One third of the maquette is a hydrophilic domain, and two-thirds is hydrophobic. Each helix has two histidines for cofactor binding in the hydrophobic domain and one in the hydrophilic domain. The maquette is soluble in methanol and other organic solvents, and it is capable of binding a variety of cofactors including the zinc(II) protoporphyrin IX (ZnPP) used here. Ultracentrifugation shows that six cofactors can be incorporated in the maquette, but some may have fewer. (see Figure 4 in the Methods and Materials section).

An idealized protein–electrode junction configuration was fabricated (Figure 1C). Self-assembled layers of protein maquettes were patterned on atomically smooth highly oriented pyrolytic graphite (HOPG) using microcontact printing.[18–21] The first layer of the amphiphilic proteins will orient on the hydrophobic graphite with the hydrophobic domain nearest the graphite due to hydrophobic interactions. A single molecular layer is identified when the height of the patterned region is 6.6 ± 0.5 nm, the length of a 4-helix bundle. In these regions, the proteins must be standing up; that is, no combination of other orientations results in this dimension. Though the tilt angle is not determined and the in-plane ordering is not known, the molecule must be vertically aligned on the metallic graphite substrate.

The challenges of characterizing biomolecule interfaces are a consequence of the complexity and delicate nature of the structure. It would be of particular value to probe a complex property such as impedance which, in contrast to conductance, contains information about both the real and imaginary components of the response. Combining impedance with an optical probe would provide access to molecular and interface polarization, as well as transport and photoconduction. However, many approaches available for hard surfaces cannot be employed on biomolecules. Consequently, most previous characterization has been done in solution through electrochemical techniques such as electrochemical impedance spectroscopy or cyclic voltametry.[1,22–26] For example, similar maquettes on electrodes have been studied in liquid.[15–17] Recently, some progress has been made with SPM techniques, either through self-assembled monolayers (SAMS) examined with scanning tunneling microscopy[27–31] or with liquid-cell atomic force microscopy techniques.[32–37] In order to achieve property characterization that requires probe–tip contact to the biomolecules, extreme control of the forces involved is required.

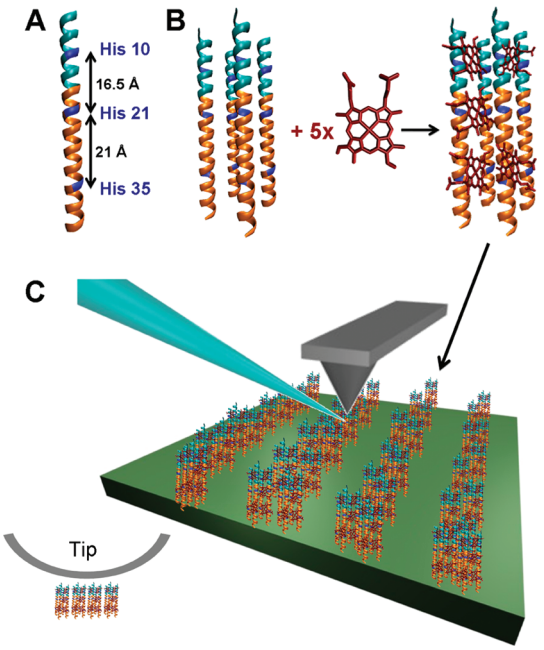

Figure 1. Design strategy. (A) α-Helix of a maquette illustrating the locations of the binding sites (histidines, dark blue). Light blue indicates hydrophilic domains; yellow indicates hydrophobic domains. The entire α-helix is 66 Å long. His10 is in the hydrophilic domain, and His21 and His35 are in the hydrophobic domain. The peptide sequence is CGGGEIWKQHEEALKKFFAFHFILPFIIMAIA-MAHLLFLFGEGL. (B) Model of 4-helix bundle. The width of the entire bundle is 2.5 nm. Five ZnPP (red) are added per 4-helix bundle. (C) Idealized protein–electrode junction device configuration. The substrate is HOPG. The maquettes are oriented perpendicular to the underlying substrate. A 425 nm LED (blue) is directed at the tip–sample junction.

A new scanning probe technique, torsional resonance nanoimpedance microscopy, was developed to measure properties in ambient conditions on electrode substrates. Torsional resonance is employed to control the sample–tip force interaction and topographic imaging, enabling near-field contact with the lowest possible (10 nN) force. An impedance measurement system is designed to operate at very low currents typical for SAMs (<1 pA), operate over a significant frequency range (kHz to 100 kHz) in order to increase signal-to-noise ratios, and compensate for system stray capacitances. A 425 nm LED is used for optical excitation (see Figure 5 in the Methods and Materials section). Impedance, Z, is defined as the ratio of the AC voltage excitation, V, to a current response, I: $Z(\omega) = V(\omega)/I(\omega)$, where ω is the frequency of the AC signal. Impedance Z is usually expressed in complex form in terms of its modulus, $|Z|$, and phase, θ, as $Z = |Z|e^{i\theta}$. Z is a function of frequency, ω, because processes such as ionic flux and electron trapping respond with different time constants.[38–40] These relations illustrate that an advantage of the frequency modulated approach is that both real and imaginary components of the properties are accessed.

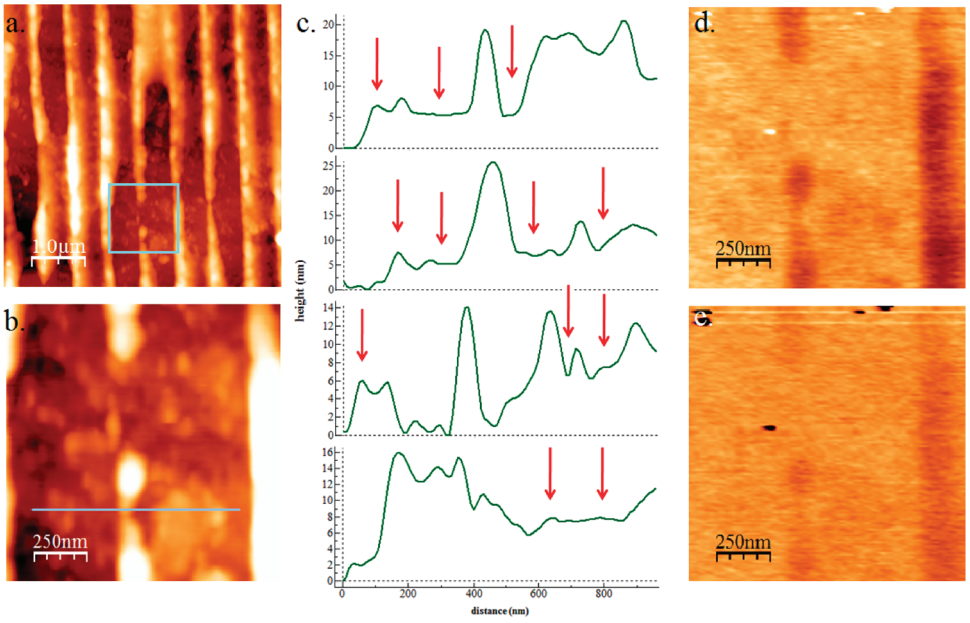

Figure 2. Proteins patterned on an electrode. ZnPP maquettes, 20 μL, 30 μM, 15 s stamping time. (a) Topography, (b) zoomed in area of box in (a), (c) profiles of various areas of ZnPP maquettes. The first line profile corresponds to the line in image (b). Red arrows indicate regions of ~6.6 nm, which are one monolayer in height. (d) *x*-Component of impedance of area in (b), (e) *y*-component of impedance in (b). The *x* and *y* *z*-range = 125 mV, height *z*-range = 90 nm in (a) and 40 nm in (b); 70 kHz, 0.5 V applied signal.

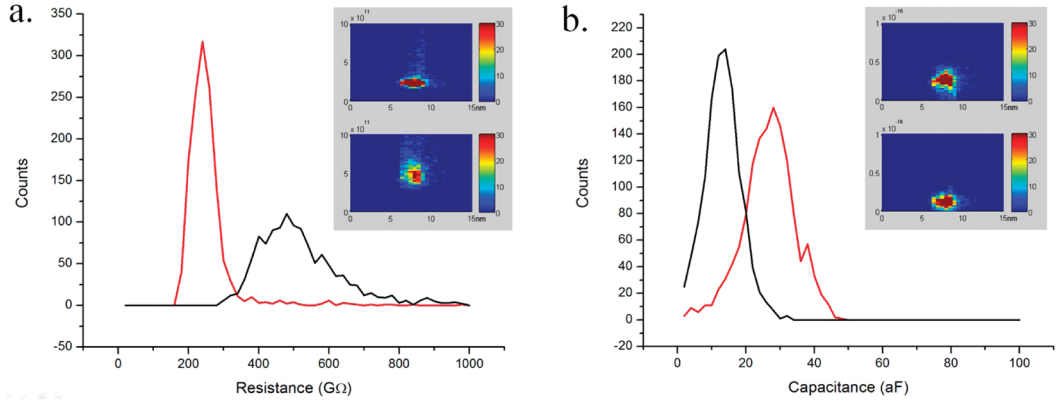

Figure 3. Effect of optical illumination on the resistance (a) and capacitance (b) of monolayer ZnPP maquettes illustrated as 2D and 3D histograms of the properties. The top 3D histograms in the insets are the properties with illumination, the bottom without illumination. Red curves in the 2D histograms are with illumination, black curves are without exposure; λ = 425 nm.

Figure 2 presents a typical spatially resolved impedance measurement. The topographic structures shown in Figure 2a,b are typical of a protein patterned electrode, in this case, with a pattern pitch of 1 μm and protein lines varying in height from 6 to 20 nm. The patterns with heights of >7 nm obviously consist of multiple molecular layers with complex structure and are not considered further here. Many regions of the patterns exhibit heights very close to 6.6 nm, the length of a single 4-helix bundle. These regions, in which the orientation of the molecule with respect to the substrate can be assigned, are identified by height profiles in the range of 6.6 $\pm$ 0.5 nm, and the impedance is analyzed. Figure 2c identifies several such regions. Note that, in many regions, the monolayer film extends over hundreds of nanometers. In these samples, the monolayer alignment often occurs in the regions between the patterns. The component of the impedance related to resistance is mapped in Figure 2d, and the component related to capacitance is mapped in Figure 2e (see the Methods and Materials section for the quantitative relationships). Measurements made during optical excitation with 425 nm light were similar to those in Figure 2d,e but differed in magnitudes.

Figure 3 compares several hundred values of the resistance (a) and capacitance (b) in a region of the ZnPP monolayer that statistically verifies the differences observed upon photoexcitation. The 3D histograms illustrate the molecular height range around 6.6 nm that are included in the analysis. There is a

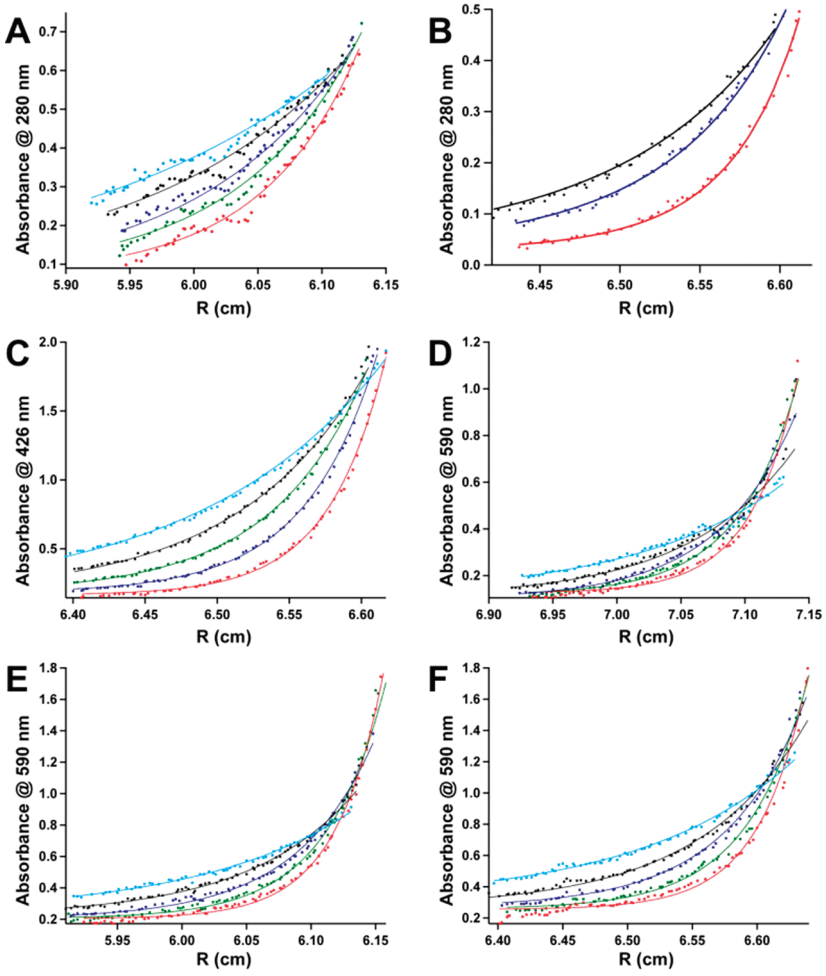

Figure 4. Sedimentation equilibrium profiles of AP6 without cofactor (A,B) and AP6 with 2 ZnPP (C), 4 ZnPP (D), 8 ZnPP (E), and 12 ZnPP (F) in methanol (A) and in 10 mM DPC (B−F). The samples were equilibrated at five different speeds: 25k rpm (cyan), 30k rpm (black), 35k rpm (navy blue), 40k rpm (green), and 45k rpm (red).

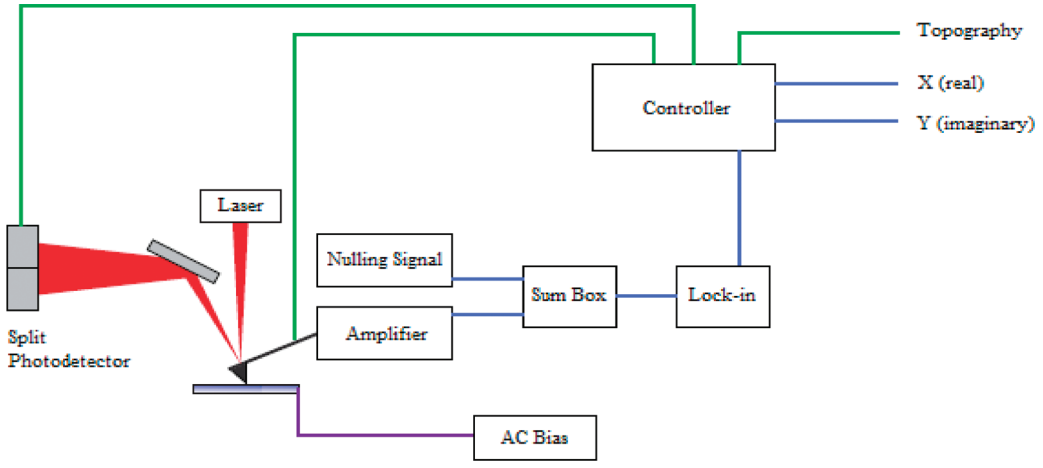

Figure 5. Torsional resonance nanoimpedance microscopy schematic. An AC bias is applied to the tip/sample, and the alteration in this signal due to the impedance of the sample is output to the amplifier. The signal from the amplifier is summed with the compensating signal to account for the capacitance of the entire system. The summed signals enter the lock-in amplifier. The output of the lock-in amplifier is fed into the microscope controller for analysis.

small ~1 nm offset is these analyses, but the approach has the advantage of extracting hundreds of measurements to yield a statistically valid result. The reduction of resistance and increase in capacitance is clear. We note that not all regions that appear to be monolayers exhibit this magnitude of dependence, a fact that we

attribute to variations in the local structure and cofactor content.

DISCUSSION

The resistance is a measure of electron transport through the ZnPP maquettes, which in helices is a complex process. Transport could include hopping through the residues in the backbone, evidence of which has been extensively studied elsewhere.[24,41−44] Furthermore, even in "dry" state, water is tightly bound to the structure; otherwise, the α-helix would be deformed without its stabilizing effect. A contribution to current could arise from transport through these water-containing sites.[5,6] Finally, the peptides are designed to enable tunneling to the porphyrins even in the dark state. It is unsurprising that optical excitation results in a decrease in the resistance of the protein/electrode pattern at both 70 and 100 kHz. The ZnPP cofactors are known to be photoactive and were, in fact, used here specifically to impart this behavior. Photoactivity is preserved upon binding into a 4-helix bundle. The average resistance in the presence of light is 2 times less than the dark resistance (Figure 3). Optical absorption excites electrons into the S1 and S2 states, the second of which decays with a femtosecond time constant into the S1 state, which has a nanosecond relaxation time. Optical absorption causes an increase in the number of charge carriers that reside in delocalized states which can open an additional transport path.[45] The other potential transport mechanisms are not expected to be photoactive, though this possibility is not ruled out in our study.

More interesting is that the capacitance of the protein/electrode structures exhibits a dependence on optical excitation. The capacitance (*C*) in the presence and absence of optical illumination is compared in Figure 3b. Interestingly, the capacitance increases upon optical absorption; it is 3 times greater than the dark values. In the absence of dimensional or quantum confinement effects, the capacitance is a direct measure of the dielectric function, which is related to molecular polarizability. Generally, to accurately extract the dielectric constant from the capacitance of the probe−surface configuration, a complex function involving the tip shape and height, which must be known, is required.[46,47] Here we are interested in the change in dielectric constant upon excitation. Since the geometric factors are held constant, a simpler analysis is sufficient to quantify the differences in properties. For an estimate of the dielectric permittivity, we assume that the system is a parallel plate capacitor. Adhesive forces between the tip and the sample imply contact between the tip and the sample; the contact area is typically smaller than the tip radius, which is 40 nm. However, the presence of an aqueous meniscus, which is larger and acts as a conductor, means that the top plate of the capacitor can be assumed to be an 80 nm diameter disk.[48] The dielectric constant resulting from this analysis for ZnPP maquette patterns changes from 1.17 ± 0.47 in the zabsence of light to 2.54 ± 0.52 upon optical excitation. The dark values are within the range expected for organic films.

We consider two possible mechanisms for the increased dielectric constant on optical excitation. Either the polarizability of the cofactors reinforces the dipole of the peptide helices or the change in polarizability volume of the porphyrins directly affects the capacitance. A change in polarization reflects differences between the excited state and ground state dipole moment—both the permanent dipole moment and the field-induced dipole moment, which is a product of the applied electric field and the change in molecular polarizability volume. For Zn porphyrin molecules, no measurable change in ε'' (the dielectric loss) is observed on optical excitation, indicating that the excited states have no dipolar character, as might be expected on the basis of symmetry.[49] Incorporation into the α-helices does not produce a dipole within the cofactor.

It is known, however, that photoexcitation increases the polarizability volume of porphyrin molecules. The excited state polarizability volume is related qualitatively to exciton delocalization.[49−52] She *et al.* used transient photoconductivity in liquid and found the photoinduced polarizability change is 60 ± 20 Å^3, from 90 to 150 ± 20 Å^3 for both singlet and triplet states, for a ZnPP molecule. Piet *et al.* found the same value from time-resolved microwave conductivity, also in solution. Monomers exhibit somewhat smaller changes, and extensive coupling in larger complexes yields larger changes. For the cofactor−maquette monolayers attached to a substrate, the data correspond to an increase of 117−267% in polarizability volume. The agreement between the single cofactor and cofactor−maquette indicates that the photoinduced change in dielectric constant is primarily due to excited state polarization volume increase.

This result has several implications. First, the protein design was successful in producing a photoactive structure that can be attached to an electrode in dry ambient environments, and the optical properties of the porphyrin are not negatively altered by attachment to the peptide or the electrode. Since the peptide can be designed to attach this and other porphyrins at various positions within the helix, a wide range of device properties can be envisioned. Second, probing excited state molecular polarizability provides a direct indication of exciton delocalization, a property critical to optoelectronic properties.

CONCLUSION

In summary, protein design was used to fabricate device-like configurations with optoelectronic function. The combination of a new probe of optical

dielectric function in biomolecules and careful design of proteins enables mechanisms of electronic transport and optoelectronic function to be simultaneously examined. In this specific case, the excited state polarizability of a protein complex was quantified at the single molecular layer level in a manner that can map spatial variations. This is possible by probing both the real and imaginary components of the properties and allows an important observation of photoactivity of an engineered protein/electrode system in ambient conditions. These results will pave the way for understanding materials properties of biological molecules bound to ambient electrodes, with potential applications in sensors and photovoltaics.

TABLE 1. Partial Specific Volume of AP6/ZnPP Complexes[a]

sample	partial specific vol	expected MW	apparent MW
AP6 in methanol	0.7693	5022	4954 ± 170
AP6	0.7693	20088	20927 ± 65
AP6 + 2 ZnPPIX	0.7723	21340	23430 ± 81
AP6 + 4 ZnPPIX	0.7749	22592	23762 ± 178
AP6 + 8 ZnPPIX	0.7773	23844	28125 ± 159
AP6 + 12 ZnPPIX	0.7773	23844	25808 ± 139

[a] Weight average of AP6 and ZnPP.

METHODS AND MATERIALS

Peptide Synthesis and Purification. The AP6 peptides with the following sequence CGGGEIWKQ**H**EEALKKFFAF**H**FILPFIIMAIAMA**H**LLFLFGEGL were synthesized at 0.1 mmol scale on a Liberty solid phase peptide synthesizer (CEM) using an Fmoc-PEG-PAL-PS resin (NovaBioChem) and Fmoc-protected amino acids (NovaBioChem). The peptides were purified on a reversed-phase C18 HPLC column (Vydac) using gradients of acetonitrile (Fisher) and water both containing 0.1% (v/v) trifluoroacetic acid (Sigma). The purity and molecular weight of the AP6 peptide was confirmed by matrix-assisted laser desorption/ionization mass spectrometry (MALDI-MS) to be 5022 g/mol. The peptides were purified without difficulty with yields comparable to water-soluble peptides of similar length.

The peptide was solubilized in methanol in submillimolar concentrations, diluted approximately 10× with dichloromethane, and co-solubilized with ZnPP. Analytical ultracentrifugation experiments confirmed that the AP6 maquettes assemble in 10 mM DPC as tetramers; therefore; the word maquette refers to the total assembly of four peptide helices. As such, our peptide concentrations reported here are for assembled 4-helix bundles. Peptide concentrations were determined by UV−visible absorbance spectroscopy at 280 nm assuming an extinction coefficient of 22 400 M^{-1} cm^{-1} $bundle^{-1}$ calculated from the AP6 sequence using the Swiss Institute of Bioinformatics' EXPASY server (http://us.expasy.org/cgi-bin/protparam).

Analytical Ultracentrifugation. The association states of the peptide and Zn protoporhyrin IX/peptide complexes in methanol and in 10 mM DPC (dodecyl phosphatidylcholine, Avanti Polar Lipids) were determined at 25 °C using an analytical ultracentrifuge (Beckman XL-I, Beckman Coulter). To determine self-assembly in methanol, the peptides were dissolved directly into methanol to 20 μM concentration. For assembly in aqueous solutions, peptide was dissolved in 25 mM DPC and diluted into solution containing 20 μM peptide, 20 mM phosphate buffer (pH = 8.0), 100 mM KCl, 51% D_2O (empirically determined to match the density of the DPC detergent), and specified equivalents of Zn protoporphyrin IX. The sedimentation profiles at different speeds (25, 30, 35, 40, and 45 krpm) were analyzed by global curve-fitting of radial concentration gradients (measured using optical absorption at 280, 426, and 550 nm) to the sedimentation equilibrium equation.

Confirmation of 4-Helix Bundle Formation through Analytical Ultracentrifugation. ZnPP binding to AP6 maquettes dissolved in detergent does not produce a significant shift or increase in the ZnPP absorbance, and therefore, binding of ZnPP to AP6 cannot be confirmed by UV−vis spectroscopy. Therefore, we have used analytical ultracentrifugation to establish that the ZnPP binds to AP6. The sedimentation equilibrium profiles were fitted with equation for equilibrium of single species with unknown apparent molecular weight. The partial specific volume for AP6 was calculated based on the amino acid sequence using program Sednterp downloaded from http://www.rasmb.bbri.org/software. The partial specific volume of ZnPP was considered to be identical to partial specific volume of heme, 0.82 mL/g. The partial specific volume of AP6/ZnPP complex was calculated as weight average of AP6 and ZnPP (Table 1). The apparent molecular weight of AP6 dissolved in methanol is in very good agreement with the molecular weight of AP6 monomer, and the apparent molecular weight of AP6 solubilized in 10 mM DPC is in very good agreement with AP6 assembled into tetramers (Table 1). The sedimentation equilibrium profiles measured at 426 and 590 nm indicate that the ZnPP associates with AP6. The absorbance at 426 nm increased above the linear detection level of the spectrophotometer when 4 or more ZnPP were added per one AP6 maquette. Absorbance at 590 nm stayed in the linear detection regime, but it increased only 50% from 4 ZnPP to 8 ZnPP, and it did not increase any higher when more equivalents of ZnPP per maquette were added, which indicates that only 6 ZnPP molecules bind to AP6 maquette. The apparent molecular weight determined upon additions of 2, 4, 8, and 12 ZnPP is also in agreement with AP6 assembly into tetramers that bind up to 6 ZnPP. The slight increase (up to 15%) in apparent molecular weight might be due to small error in the density match and/or variability of the partial specific volume of any of the three species (AP6, ZnPP, and/or DPC) upon assembly.

Protein Pattern Fabrication on Metallic Electrodes. The silicone polymer (Sylgard 184 Silicone Encapsulant) starting materials were mixed according to manufacturer's (Ellsworth Adhesives) specifications and poured over a diffraction grating (grating with 1200 grooves/mm, Optometrics) and placed overnight at 80 °C in an oven. The cured polymer (henceforth called stamps) was peeled off the grating and cut into pieces that were approximately 10 mm × 10 mm. The new stamps were washed according to a previously published methodology using hexane and 2-propanol and oven-dried overnight at 80 °C. A fresh stamp was used for each stamping step, and used stamps were sonicated in hexane (10 min) and 2-propanol (2× 2-propanol for 5 min each) and oven-dried overnight at 80 °C prior to reusing.

The ink (ZnPP maquettes in CH_2Cl_2) concentration for stamping was 30 μM, and an ink volume of 1.5−20 μL was deposited on the stamp using a micropipet, dried with ultrahigh pure N_2 gas, and brought into contact with the substrate for 2−10 s. The HOPG (Mikromasch) was freshly peeled prior to stamping.

Torsional Resonance Nanoimpedance Microscope (TR-NIM) for Optoelectronic Properties. In torsional mode, the probe was oscillated along the cantilever's long axis, creating a rotational oscillation. AFM measurements at torsional resonances provided a key advantage: the ability to achieve low-force scanning while maintaining the tip in the near-field. As a result, it is possible to measure tunneling currents between the tip and sample without damaging the sample. Figure 5 illustrates a schematic diagram of the TR-NIM configuration. The tip was maintained in proximity of the sample surface by the microscope controller. The electrical impedance of tip−surface junction was

measured using external circuitry consisting of a current amplifier, signal generator, and lock-in amplifier. Tunneling currents across biological molecules were quite small; in order to measure this current, a high-speed and high-gain current amplifier was required. The signal generator and current amplifier have a common ground. A reference signal was fed into the lock-in amplifier for synchronization of signal generator and lock-in amplifier. This setup worked in the frequency range from 1 Hz to 1 MHz, though this limit was set only by available equipment.

For TR-NIM experiments, a platinum−iridium-coated tip was used; f_o = 146−236 kHz and k = 21−98 N/m (Nanosensors). The AFM measurements were performed on a Veeco Dimension 3100 with IVa controller modified with a home-built impedance spectroscopy circuit designed to account for signal-to-noise and stray signal compensation. Two current amplifiers were used which together provide a gain range of 1×10^2 to 1×10^{11} V/A (Femto DLPCA-200, DHPCA-100). Two lock-in amplifiers provided a frequency range from ~1 mHz to 200 MHz (SRS830, SRS844). The AC signal was applied at either 70 or 100 kHz (SRS DS345).

The total impedance can be modeled as the impedance due to capacitive coupling, which is the impedance due to the system, and the impedance of the sample. It is assumed that the impedances are in parallel. The compensating signal coming out of the slave signal generator is set to account for capacitance of the system. In order to achieve that, before scanning begins, the slave is adjusted so that the total voltage coming out of the sum box is as close to zero as possible. The summation of the canceling signal with the output signal was monitored with an oscilloscope (Tektronix).

In this circuit the impedance, Z, is

$$Z_s = 10\sqrt{2}\frac{VG}{sV_o}$$

where V = applied voltage, s = sensitivity, V_o = output of lock-in amplifier, and G = gain of amplifier, s = sensitivity ($\sqrt{2}$ because V_o is rms voltage, 10 is a conversion factor within the lock-in amplifier).

Assuming the molecule can be represented as an RC circuit

$$R = \frac{10\sqrt{2}VG}{sX} \quad C = \frac{sY}{10\sqrt{2}VG\omega}$$

where ω = frequency. The data were acquired with the following parameters: V = 0.5 V, gain = 10^6 or 10^7, ω = 70 or 100 kHz, s = 5, 10, 20, or 30 mV. The values for X and Y are relative to that of the graphite. If the compensating signal is perfect, we measure zero impedance over graphite. The change in impedance is then entirely attributed to the molecule.

Light experiments were done with a 425 nm diode set at a glancing angle (Prizmatix LED). The diode was directed at the tip−surface junction. A micromanipulator (Thorlabs MBT4OZ) on the stage assisted in accurate positioning of the diode. The AFM instrumentation had been encased with a black-out tent for dark measurements. Control experiments were done on CdTe, where we obtained dielectric constant values in agreement with those reported in the literature.

Acknowledgment. The authors acknowledge support from the Nano/Bio Interface Center under NSF Grant DMR08-32802 and use of the NanoProbe Facility. We are grateful to Stephen Nonneman for assistance with figures, and Xi Chen for contribution to analysis.

REFERENCES AND NOTES

1. Frolov, L.; Rosenwaks, Y.; Carmeli, C.; Carmeli, I. Fabrication of a Photoelectronic Device by Direct Chemical Binding of the Photosynthetic Reaction Center Protein to Metal Surfaces. *Adv. Mater.* **2005**, *17*, 2434–2437.
2. Lee, I.; Lee, J. W.; Stubna, A.; Greenbaum, E. Measurement of Electrostatic Potentials above Oriented Single Photosynthetic Reaction Centers. *J. Phys. Chem. B* **2000**, *104*, 2439–2443.
3. Engel, A.; Shoenenberger, C.-A.; Muller, D. J. High Resolution Imaging of Native Biological Sample Surfaces Using Scanning Probe Microscopy. *Curr. Opin. Struct. Biol.* **1997**, *7*, 279–284.
4. Colton, R. J.; Baselt, D. R.; Dufrene, Y. F.; Green, J.-B. D.; Lee, G. U. Scanning Probe Microscopy. *Curr. Opin. Chem. Biol.* **1997**, *1*, 370–377.
5. Moser, C. C.; Anderson, J. L.; Dutton, P. L. Guidelines for Tunneling in Enzymes. *Biochim. Biophys. Acta* **2010**, *1797*, 1573–1586.
6. Page, C. C.; Moser, C. C.; Chen, X.; Dutton, P. L. Natural Engineering Principles of Electron Tunneling in Biological Oxidation−Reduction. *J. Am. Chem. Soc.* **1999**, *127*, 47–52.
7. Cochran, F. V.; Wu, S. P.; Wang, W.; Nanda, V.; Saven, J. G.; Therien, M. J.; DeGrado, W. F. Computational *De Novo* Design and Characterization of a Four-Helix Bundle Protein That Selectively Binds a Non-biological Cofactor. *J. Am. Chem. Soc.* **2005**, *127*, 1346–1347.
8. DeGrado, W.; Summa, C. M.; Pavone, V; Nastri, F; Lombardi, A. *De Novo* Design and Structural Characterization of Proteins and Metalloproteins. *Annu. Rev. Biochem.* **1999**, *68*, 779–819.
9. Cordova, J. M.; Noack, P. L.; Hilcove, S. A.; Lear, J. D.; Ghirlanda, G. Design of a Functional Membrane Protein by Engineering a Heme-Binding Site in Glycophorin A. *J. Am. Chem. Soc.* **2006**, *129*, 512–518.
10. Ghirlanda, G. Design of Membrane Proteins: Toward Functional Systems. *Curr. Opin. Chem. Biol.* **2009**, *13*, 643–651.
11. Ye, S. X.; Discher, B. M.; Strzalka, J.; Xu, T.; Wu, S. P.; Noy, D.; Kuzmenko, I.; Gog, T.; Therien, M. J.; Dutton, P. L.; *et al.* Amphiphilic Four-Helix Bundle Peptides Designed for Light-Induced Electron Transfer across a Soft-Interface. *Nano Lett.* **2005**, *5*, 1658–1667.
12. Discher, B. M.; Noy, D.; Strzalka, J.; Ye, S. X.; Moser, C. C.; Lear, J. D.; Blasie, J. K.; Dutton, P. L. Design of Amphiphilic Protein Maquettes: Controlling Assembly, Membrane Insertion, and Cofactor Interactions. *Biochemistry* **2005**, *44*, 12329–12343.
13. Noy, D.; Discher, B.; Rubstov, I.; Hochstrasser, R.; Dutton, P. L. Design of Amphiphilic Protein Maquettes: Enhancing Maquette Functionality through Binding of Extremely Hydrophobic Cofactors to Lipophilic Domains. *Biochemistry* **2005**, *44*, 12344–12354.
14. Shifman, J. M.; Moser, C. C.; Kalsbeck, W. A.; Bocian, D. F.; Dutton, P. L. Functionalized *De Novo* Designed Proteins: Mechanism of Proton Coupling to Oxidation/Reduction in Heme Protein Maquettes. *Biochemistry* **1998**, *37*, 16815–16827.
15. Pilloud, D. L.; Chen, X.; Dutton, P. L.; Moser, C. C. Electrochemistry of Self-Assembled Monolayers of Iron Protoporphyrin IX Attached to Modified Gold Electrodes through Thioether Linkage. *J. Phys. Chem. B* **2000**, *104*, 2868–2877.
16. Chen, X. X.; Discher, B. M.; Pilloud, D. L.; Gibney, B. R.; Moser, C. C.; Dutton, P. L. *De Novo* Design of a Cytochrome B Maquette for Electron Transfer and Coupled Reactions on Electrodes. *J. Phys. Chem. B* **2002**, *106*, 617–624.
17. Topoglidis, E.; Discher, B. M.; Moser, C. C.; Dutton, P. L.; Durrant, J. R. Functionalizing Nanocrystalline Metal Oxide Electrodes with Robust Synthetic Redox Proteins. *ChemBioChem* **2003**, *4*, 1332–1339.
18. Wilbur, J. L.; Kumar, A.; Biebuyck, H. A.; Kim, E.; Whitesides, G. M. Microcontact Printing of Self-Assembled Monolayers: Applications in Microfabrication. *Nanotechnology* **1996**, *7*, 452–457.
19. Kumar, A.; Abbot, N. L.; Kim, E.; Biebuyck, H. A.; Whitesides, G. M. Patterned Self-Assembled Monolayers and Mesoscale Phenomena. *Acc. Chem. Res.* **1995**, *28*, 219–226.
20. Kumar, A.; Whitesides, G. M. Features of Gold Having Micrometer to Centimeter Dimensions Can Be Formed through a Combination of Stamping with an Elastomeric Stamp and an Alkanethiol Ink Followed by Chemical Etching. *Appl. Phys. Lett.* **1993**, *63*, 2002–2004.

21. Kane, R. S.; Takayama, S.; Ostuni, E.; Ingber, D. E.; Whitesides, G. M. Patterning Proteins and Cells Using Soft Lithography. *Biomaterials* **1999**, *20*, 2363–2376.
22. Raguse, B.; Braach-Maksvytis, V.; Cornell, B. A.; King, L. G.; Osman, P. D. J.; Pace, R. J.; Wieczorek, L. Tethered Lipid Bilayer Membranes: Formation and Ionic Reservoir Characterization. *Langmuir* **1998**, *14*, 648–659.
23. Ron, I.; Sepunaru, L.; Itzhakov, S.; Belenkova, T.; Friedman, N.; Pecht, I.; Sheves., M.; Cahen, D. Proteins as Electronic Materials: Electron Transport through Solid-State Protein Monolayer Junctions. *J. Am. Chem. Soc.* **2010**, *132*, 4131–4140.
24. Mandal, H. S.; Kraatz, H.-B. Electron Transfer across α Helical Peptides: Potential Influence of Molecular Dynamics. *Chem. Phys.* **2006**, *326*, 246–251.
25. Davis, J. J.; Morgan, D. A.; Wrathmell, C. L.; Axford, D. N.; Zhao, J.; Wang, N. Molecular Bioelectronics. *J. Mater. Chem.* **2005**, *15*, 2160–2174.
26. Shinwari, M. W.; Deen, M. J.; Starikov, E. B.; Cuniberti, G. Electrical Conductance in Biological Molecules. *Adv. Funct. Mater.* **2010**, *20*, 1865–1883.
27. Kitagawa, K.; Morita, T.; Kimura, S. Electron Transport Properties of Helical Peptide Dithiol at a Molecular Level: Scanning Tunneling Microscope Study. *Thin Solid Films* **2006**, *509*, 18–26.
28. Kitagawa, K.; Morita, T.; Kawasaki, M.; Kimura, S. Electron Transfer in Metal−Molecule−Metal Junction Composed of Self-Assembled Monolayers of Helical Peptides Carrying Redox-Active Ferrocene Units. *Langmuir* **2005**, *21*, 10624–10631.
29. Kitagawa, K.; Morita, T.; Kawasaki, M.; Kimura, S. Electric Properties of Self-Assembled Monolayers of Helical Peptides by Scanning Tunneling Spectroscopy. *J. Polym. Sci., Part A: Polym. Chem.* **2003**, *41*, 3493–3500.
30. Carmeli, I.; Frolov, L.; Carmeli, C.; Richter, S. Photovoltaic Activity of Photosystem I-Based Self-Assembled Monolayer. *J. Am. Chem. Soc.* **2007**, *129*, 12352–12353.
31. Moore, A. M.; Yeganeh, S.; Yao, Y. X.; Claridge, S. A.; Tour, J. M.; Ratner, M. A.; Weiss, P. S. Polarizabilities of Adsorbed and Assembled Molecules: Measuring the Conductance through Buried Contacts. *ACS Nano* **2010**, *4*, 7630–7636.
32. Casuso, I.; Fumagalli, L.; Samitier, J.; Padros, E.; Reggiani, L.; Akimov, V.; Gomila, G. Nanoscale Electrical Conductivity of the Purple Membrane Monolayer. *Phys. Rev. E* **2007**, *76*, 041919.
33. Hawkins, A. R.; Liu, H.; Oliphant, T. E.; Schultz, S. M. Noncontact Scanning Impedance Imaging in an Aqueous Solution. *Appl. Phys. Lett.* **2004**, *85*, 1080–1082.
34. Oliphant, T. E.; Liu, H.; Hawkins, A. R.; Schultz, S. M. Simple Linear Models of Scanning Impedance Imaging for Fast Reconstruction of Relative Conductivity of Biological Samples. *IEEE Trans. Biomed. Eng.* **2006**, *53*, 2323–2331.
35. Fumagalli, L.; Ferrari, G.; Sampietro, M.; Gomila, G. Quantitative Nanoscale Dielectric Microscopy of Single-Layer Supported Biomembranes. *Nano Lett.* **2009**, *9*, 1604–1608.
36. Casuso, I.; Fumagalli, L.; Samitier, J.; Padros, E.; Reggiani, L; Akimov, V.; Gomila, G. Electron Transport through Supported Biomembranes at the Nanoscale by Conductive Atomic Force Microscopy. *Nanotechnology* **2007**, *18*, 465503.
37. Casuso, I.; Fumagalli, L.; Gomila, G.; Padros, E. Nondestructive Thickness Measurement of Biological Layers at the Nanoscale by Simultaneous Topography and Capacitance Imaging. *Appl. Phys. Lett.* **2007**, *91*, 063111.
38. Shao, R.; Kalinin, S. V.; Bonnell, D. A. Local Impedance Imaging and Spectroscopy of Polycrystalline ZnO Using Contact Atomic Force Microscopy. *Appl. Phys. Lett.* **2003**, *82*, 1869–1871.
39. Shao, R.; Bonnell, D. A. Scanning Probes of Nonlinear Properties in Complex Materials. *Jpn. J. Appl. Phys.* **2004**, *43*, 4471–4476.
40. Pingree, L. S. C.; Hersam, M. C. Bridge-Enhanced Nanoscale Impedance Micoscopy. *Appl. Phys. Lett.* **2005**, *87*, 233117.
41. Long, Y. T.; Abu-Irhayem, E.; Kraatz, H. B. Peptide Electron Transfer: More Questions Than Answers. *Chem.—Eur. J.* **2005**, *11*, 5186–5194.
42. Yanagisawa, K.; Morita, T.; Kimura, S. Efficient Photocurrent Generation by Self-Assembled Monolayers Composed of 3_{10} Helical Peptide Carrying Linearly Spaced Naphthyl Groups at the Side Chains. *J. Am. Chem. Soc.* **2004**, *126*, 12780–12781.
43. Winkler, J. R.; Gray, H. B. Electron Tunneling in Proteins: Role of the Intervening Medium. *J. Biol. Inorg. Chem.* **1997**, *2*, 399–404.
44. Striplin, D. R.; Reece, S. Y.; McCafferty, D. G.; Wall, C. G.; Friesen, D. A.; Erickson, B. W.; Meyer, T. J. Solvent Dependence of Intramolecular Electron Transfer in a Helical Oligoproline Assembly. *J. Am. Chem. Soc.* **2004**, *126*, 5282–5291.
45. Jin, Y. D.; Friedman, N.; Sheves, M; He, T.; Cahen, D. Bacteriorhodopsin (bR) as an Electronic Conduction Medium: Current Transport through bR-Containing Monolayers. *Proc. Natl. Acad. Sci. U.S.A.* **2006**, *103*, 8601–8606.
46. Brukman, M., Bonnell, D. High Sensitivity, High Resolution Dielectric Mapping of Thin Films. *Nanotechnology*, Submitted for publication.
47. Hudlet, S.; Jean, M. S.; Guthmann, C.; Berger, J. Evaluation of the Capacitive Force between an Atomic Force Microscopy Tip and a Metallic Surface. *Eur. Phys. J. B* **1998**, 2.
48. Lee, D. T.; Pelz, J. P.; Bhushan, B. Scanning Capacitance Microscopy for Thin Film Measurements. *Nanotechnology* **2006**, *17*, 1484–1491.
49. Piet, J. J.; Taylor, P. N.; Anderson, H. L.; Osuka, A.; Warman, J. M. Excitonic Interactions in the Singlet and Triplet Excited States of Covalently Linked Zinc Porphyrin Dimers. *J. Am. Chem. Soc.* **2000**, *122*, 1749–1757.
50. Piet, J. J.; Taylor, P. N.; Wegewijs, B. R.; Anderson, H. L.; Osuka, A.; Warman, J. M. Photoexcitations of Covalently Bridged Zinc Porphyrin Oligomers: Frenkel *versus* Wannier-Mott Type Excitons. *J. Phys. Chem. B* **2001**, *105*, 97–104.
51. She, C.; McGarrah, J. E.; Lee, S. J.; Goodman, J. L.; Nguyen, S. T.; Williams, J. A. G.; Hupp, J. T. Probing Exciton Localization/Delocalization: Transient DC Photoconductivity Studies of Excited States of Symmetrical Porphyrin Monomers, Oligomers, and Supramolecular Assemblies. *J. Phys. Chem. A* **2009**, *113*, 8282–8186.
52. Huang, S. S.; Koder, R. L.; Lewis, M.; Wand, A. J.; Dutton, P. L. The HP-1 Maquette: From an Apoprotein Structure to a Structured Hemoprotein Designed To Promote Redox-Coupled Proton Exchange. *Proc. Natl. Acad. Sci. U.S.A.* **2004**, *101*, 5536–5541.